Helicity dynamics in stratified turbulence in the absence of forcing

C. Rorai,[1,2] D. Rosenberg,[3] A. Pouquet,[1,4] and P. D. Mininni[1,5]

[1]*National Center for Atmospheric Research, P. O. Box 3000, Boulder, Colorado 80307, USA*

[2]*ICTP, Strada Costiera 11, 34151 Trieste, Italy*

[3]*National Center for Computational Sciences, Oak Ridge National Laboratory, P. O. Box 2008, Oak Ridge, Tennessee 37831, USA*

[4]*Department of Applied Mathematics, CU, Boulder, Colorado 80309-256 USA*

[5]*Departamento de Física, Facultad de Ciencias Exactas y Naturales, Universidad de Buenos Aires & IFIBA, CONICET,
Ciudad Universitaria, 1428 Buenos Aires, Argentina*

A numerical study of decaying stably stratified flows is performed. Relatively high stratification (Froude number $\approx 10^{-2}$–10^{-1}) and moderate Reynolds (Re) numbers (Re ≈ 3–6×10^3) are considered and a particular emphasis is placed on the role of helicity (velocity-vorticity correlations), which is not an invariant of the nondissipative equations. The problem is tackled by integrating the Boussinesq equations in a periodic cubical domain using different initial conditions: a nonhelical Taylor-Green (TG) flow, a fully helical Beltrami [Arnold-Beltrami-Childress (ABC)] flow, and random flows with a tunable helicity. We show that for stratified ABC flows helicity undergoes a substantially slower decay than for unstratified ABC flows. This fact is likely associated to the combined effect of stratification and large-scale coherent structures. Indeed, when the latter are missing, as in random flows, helicity is rapidly destroyed by the onset of gravitational waves. A type of large-scale dissipative "cyclostrophic" balance can be invoked to explain this behavior. No production of helicity is observed, contrary to the case of rotating and stratified flows. When helicity survives in the system, it strongly affects the temporal energy decay and the energy distribution among Fourier modes. We discover in fact that the decay rate of energy for stratified helical flows is much slower than for stratified nonhelical flows and can be considered with a phenomenological model in a way similar to what is done for unstratified rotating flows. We also show that helicity, when strong, has a measurable effect on the Fourier spectra, in particular at scales larger than the buoyancy scale, for which it displays a rather flat scaling associated with vertical shear, as observed in the planetary boundary layer.

I. INTRODUCTION

Stratified flows are encountered in many astrophysical and geophysical settings. The ratio of inertial forces to gravitational forces is expressed by the dimensionless Froude (Fr) number: Fr $= U_0/[N L_0]$, where U_0 and L_0 are the characteristic velocity and length scale of the flow, while N is the Brunt-Väissälä frequency. The Fr number can be also thought as the ratio between the gravity wave period, $\tau_W = 1/N$, to the eddy turnover time, $\tau_{\rm NL} = L_0/U_0$. Geophysical flows are generally highly stratified: In the atmosphere, Froude numbers of the order of 10^{-1} or 10^{-2} are encountered, whereas in the oceans they can be 10 times smaller. Such flows, due to their deep connection to, and their ubiquity in, our environment have been studied and reviewed extensively for their scaling and statistical properties [1,2], as well as for their physical structures [3,4].

When waves are fast compared to turbulent eddies (Fr $\ll 1$) they can dominate the dynamics, lead to the formation of stratified layers with strong vertical gradients, and intensify mixing [5,6]. For this limiting case, a suite of approximations, simpler and easier to integrate than the primitive equations, has been developed using asymptotic expansions (see, e.g., Refs. [1,7–13]), two-point closures of turbulence [14–16], or weak turbulence statistical approaches [17–19].

While the (isotropized) gravity wave period, τ_W, is not scale dependent, the eddy turnover time, $\tau_{\rm NL}$, decreases when moving to smaller length scales. In fact, nonlinear interactions are more effective at small scales and one can define the

scale ℓ at which $\tau_{\rm NL}(\ell) = \tau_W(\ell)$. This scale is called the Ozmidov scale $L_{\rm oz}$ to be defined below, and one expects that at scales smaller than $L_{\rm oz}$, isotropy and classical turbulent scaling recover.

Gravity waves (and inertia-gravity waves when rotation is included) are essential to understand the dynamics of large scales where most of the energy resides. Under the assumption of stationarity, weak nonlinearities, weak dissipation, and negligible forcing, a balance which involves the pressure gradient and the gravity (together with the Coriolis force in the presence of rotation) is obtained. Such a concept of balance has proven useful in meteorology and oceanography, and many variants and issues have been considered to study the dynamics of synoptic scales. However, gravity waves couple nonlinearly on slow time scales, as described by the weak turbulence formalism [20,21], and undergo wave steepening and breaking [2] through resonant interactions. This leads for example to frontogenesis [22,23], as observed in the upper atmosphere or in the oceans. Overturning is also present in direct numerical simulations of stratified turbulence at high resolution and high Reynolds number [24,25]. Thus, stratified turbulence is known to play a role in the vertical mixing of deep layers in the oceans, as observed, for example, in the central Pacific ocean [26], as well as in river bends and estuaries [27].

In this study we focus on the role of helicity, the correlation between the velocity field, **u**, and the vorticity, ω, in stratified flows. Helicity has not received much attention outside the realm of astrophysics when considering the growth of

TABLE I. List of the runs, computed on grids with either $n = 256$ or $n = 512$ points per dimension. The name of the runs ("Initial **v**") indicates the initial velocity field and also summarizes some important properties (e.g., whether the Reynolds or Froude numbers were changed with respect to other runs with similar initial conditions). All these calculations have $U_0 = 0.5$, and dynamical parameters are evaluated at $t = 0$; k_0 is the wave-number range of the initial condition, ν is the viscosity and Re the Reynolds number, Fr is the Froude number, $\mathcal{R}$ the buoyancy Reynolds number, η the Kolmogorov (dissipative) length scale, L_{oz} and L_b are the Ozmidov and buoyancy length scales, and $\Delta = 2\pi/(n-1)$ is the grid resolution. Note that, in general, the Ozmidov length scale is not resolved, except for runs 5, 9 10, 15, and 16. All other runs, except also the runs without stratification (Runs 6 and 12), have buoyancy Reynolds number of order unity.

Initial **v**	k_0	ν	Re	Fr	$\mathcal{R}$	η	L_{oz}	L_b	Δ
1. TG	2–3	2.4e-04	≈3000	0.022	1.452	0.0041	0.0083	0.35	0.0246
2. TGFr/2	2–3	2.4e-04	≈3000	0.011	0.363	0.0041	0.0074	0.175	0.0246
3. ABC2C	3–4	3.0e-04	≈3000	0.022	1.452	0.0044	0.0059	0.25	0.0246
4. ABC2C2Re	3–4	1.5e-04	≈6000	0.022	2.904	0.0026	0.0059	0.25	0.0123
5. ABC2C2Fr	3–4	1.5e-04	≈6000	0.044	11.616	0.0026	0.0168	0.50	0.0123
6. ABCN0	3–4	3.0e-04	≈3000	∞	∞	0.0044	∞	∞	0.0123
7. ABC	3–4	3.0e-04	≈3000	0.022	1.452	0.0044	0.0059	0.25	0.0246
8. ABC2Re	3–4	1.5e-04	≈6000	0.022	2.904	0.0026	0.0059	0.25	0.0123
9. ABC2Fr	3–4	1.5e-04	≈6000	0.044	11.616	0.0026	0.0168	0.5	0.0123
10. ABC4Fr	3–4	3.0e-04	≈6000	0.088	46.464	0.0026	0.0474	1.0	0.0246
11. ABCFr/2	3–4	3.0e-04	≈3000	0.011	0.363	0.0044	0.0021	0.125	0.0246
12. RNDN0	3–4	3.0e-04	≈3000	∞	∞	0.0044	∞	∞	0.0123
13. RND	3–4	3.0e-04	≈3000	0.022	1.452	0.0044	0.0059	0.25	0.0246
14. RND2Re	3–4	1.5e-04	≈6000	0.022	2.904	0.0026	0.0059	0.25	0.0123
15. RND2Fr	3–4	1.5e-04	≈6000	0.044	11.616	0.0026	0.0168	0.50	0.0123
16. RND4Fr	3–4	1.5e-04	≈6000	0.088	46.464	0.0026	0.0474	1.0	0.0123
17. RNDk2	2	5.24e-04	≈3000	0.022	1.452	0.0078	0.0104	0.437	0.0246

large-scale magnetic fields [28]. It is known that Ekman pumping at solid boundaries can lead to the creation of helicity, as measured in laboratory experiments as well as in numerical simulations (see, e.g., Ref. [29]). However, for a purely rotating flow, helicity is conserved with periodic boundary conditions but such is not the case in the presence of stratification.

Helicity is estimated routinely in the atmosphere, in conjunction with convective available potential energy (CAPE) to gauge the possibility of supercell convective storms to become strong [30], and it may be a factor to take into account in the formation of hurricanes [31–33]. Taking the curl of the geostrophic balance (or in the absence of rotation, the so-called cyclostrophic balance) eliminates the pressure term and, thus, also the thermodynamics that could enter through pressure gradient coupling with density variations and, for example, moisture. Thus, considering the dynamical role of helicity in stratified turbulence may allow for a focus on the dynamics of the atmospheric wind or oceanic current through decoupling from the pressure field. Note that cyclostrophic balance implies curvature of trajectories that is not due to rotation (which is neglected here), as is also the case at low latitudes or at small scales, for example, in tornadoes [34]. Helicity spectra have also been measured in the planetary boundary layer [35]. The large scale balance that arises in the presence of both rotation and stratification is considered in Ref. [36]. It can then be shown that the creation of helicity is ensured. For $N/f \leqslant 3$, it is found to be proportional to N/f where $f = 2\Omega$, with Ω the imposed solid-body rotation.

More precisely, in this work we consider the effect of helicity in freely decaying stably stratified turbulence using direct numerical simulations. We show that energy undergoes a slow decay for fully helical Beltrami flows (ABC), that

cyclostrophic balance at large scales can play an important role in determining the decay of the flow, and that helicity has an even slower evolution when compared with the energy.

In Sec. II we recall the incompressible Boussinesq equations for a stably stratified flow and we list some characteristic length scales, dimensionless number, and energies relevant to the problem under consideration. We shortly present the numerical method used to integrate the equations, and we describe the different initial conditions imposed, reporting, in Table I, the initial parameters chosen for our calculations. In Sec. III we mainly discuss the behavior of helicity for different initial conditions, we relate it to the velocity distribution in the horizontal and vertical directions, and we interpret these results proposing a type of large-scale dissipative "cyclostrophic" balance. In what follows, we study how the combined effects of different residual helicity values, different initial conditions, and different Froude and Reynolds numbers affect the temporal decay of the total energy and the Fourier spectra for the total and potential energy and for the absolute value of helicity. Finally, our results are summarized in Sec. IV.

II. EQUATIONS AND METHODOLOGY

A. Mathematical model and relevant parameters

Stably stratified turbulence is studied here by means of the incompressible Boussinesq equations. In the presence of gravity g and absence of forcing, with θ being the potential temperature fluctuations in units of velocity, the equations read

$$\partial_t \mathbf{u} + \mathbf{u} \cdot \nabla \mathbf{u} = -\nabla P - N\theta \, e_z + \nu \Delta \mathbf{u}, \qquad (1)$$

$$\partial_t \theta + \mathbf{u} \cdot \nabla \theta = Nw + \kappa \Delta \theta, \qquad (2)$$

$$\nabla \cdot \mathbf{u} = 0; \qquad (3)$$

where w is the vertical (z) component of the velocity in the direction of gravity, P is the pressure, ν the viscosity, and κ the thermal diffusivity. In this paper we take a unit Prandtl number, $\mathrm{Pr} = \nu/\kappa = 1$. The square Brunt-Väisälä frequency is given by $N^2 = -(g/\theta)(d\bar{\theta}/dz)$, where $d\bar{\theta}/dz$ is the imposed background stratification, which is assumed to be linear. No filtering on the small scales (e.g., hyperviscosity) is applied, a normal Laplacian being used for diffusion.

In the ideal case (with $\nu = \kappa = 0$), the Boussinesq equations conserve the total (kinetic plus potential) energy,

$$\tfrac{1}{2}\langle |\mathbf{u}|^2 + \theta^2 \rangle = E_V + E_P,$$

and the pointwise potential vorticity

$$V_{\mathrm{pot}} = -N\omega_z + \boldsymbol{\omega} \cdot \boldsymbol{\nabla}\theta, \tag{4}$$

which is a material invariant.

For strong waves (or weak nonlinearities), $N \gg 1$, and the nonlinear term in equation (4) above can be neglected, i.e., we can write $V_{\mathrm{pot}} \approx V_{\mathrm{pot},L} = -N\omega_z$ (where the subscript L denotes "linearized"). In that case, the $\mathcal{L}_2$ norm of linearized V_{pot} becomes proportional to $\langle \omega_z^2 \rangle$ and is also conserved, an invariance which is preserved by the Fourier truncation of the numerical algorithm. $V_{\mathrm{pot},L}$ is then proportional to the so-called vertical enstrophy, $\langle \omega_z^2 \rangle$, a situation akin (but not identical) to the two-dimensional Euler case without stratification.

The volume integrated helicity,

$$H = \langle \mathbf{u} \cdot \boldsymbol{\omega} \rangle$$

is a topological quantity that characterizes the amount of "twist" and linkage in the flow [37]. In the 3D Euler equations, in the absence of stratification and of dissipation, helicity is an invariant, as is the kinetic energy, but in the above equations it is not. We nevertheless retain this diagnostic in order to make connections to isotropic and homogeneous turbulence and to rotating flows for which helicity is invariant as well.

Relative helicity σ_V measures the degree of alignment between velocity and vorticity, and, as such, it can be viewed as a proxy measure of the amount of nonlinearity in the flow, since $\sigma_V \sim \pm 1$ implies a Lamb vector $-\mathbf{u} \cdot \boldsymbol{\nabla}\mathbf{u} + \boldsymbol{\nabla}[u^2/2] = \mathbf{u} \times \boldsymbol{\omega} \approx 0$. Relative helicity can be expressed as

$$\sigma_V = \frac{H}{\sqrt{E_V \, Z_V}}, \tag{5}$$

where $Z_V = \langle \omega^2 \rangle$ is the so-called kinetic enstrophy, proportional to the kinetic energy dissipation when viscosity is restored. One can define similarly a potential enstrophy $Z_P = \langle |\nabla\theta|^2 \rangle$, associated with the dissipation of potential energy E_P when $\kappa \neq 0$.

Three characteristic length scales can be identified for this problem: (i) the Kolmogorov length scale η, where dissipation prevails for a Kolmogorov spectrum; (ii) the Ozmidov length scale, L_{oz}; and (iii) the buoyancy length scale L_b. For the initial conditions, these length scales are defined, respectively, as

$$\eta = \left(\frac{\nu^3 L_0}{U_0^3} \right)^{1/4}, \quad L_{\mathrm{oz}} = \frac{U_0^{3/2}}{N^{3/2}}\sqrt{\frac{1}{L_0}}, \quad L_b = \frac{2\pi U_0}{N},$$

where U_0 is the initial rms velocity, $L_0 = 2\pi/k_0$ is the initial integral scale, k_0 being the wave number where the initial excitation is centered, and $\epsilon_V \equiv dE_V/dt \approx U_0^3/L_0$ is used as an estimate of the kinetic energy dissipation rate (under the assumption that the Ozmidov scale is resolved).

Three relevant dimensionless parameters can also be identified: (i) the Reynolds number $\mathrm{Re} = U_0 L_0 /\nu$; (ii) the above-mentioned Froude number, $\mathrm{Fr} = U_0/(L_0 N)$; and (iii) the buoyancy Reynolds number $\mathcal{R} = \mathrm{Re}\mathrm{Fr}^2$.

We finally define the so-called reduced kinetic energy spectra E_V as a function of the wave numbers k, $k_\perp$, and $k_\parallel$; they are, respectively, $k = |\mathbf{k}|$, $k_\perp = |\mathbf{k}_\perp| = |\mathbf{k}|\sin\Theta$, with Θ the colatitude in Fourier space with respect to the vertical axis of unit vector $\hat{\mathbf{z}}$ and $k_\parallel$ the component of $\mathbf{k}$ in the z direction. If $U_{ij}(\mathbf{k})$ is the velocity autocorrelation function in Fourier space, we name its trace $U(\mathbf{k})$. Under the assumption of homogeneity we define the axisymmetric kinetic energy spectrum as

$$e(|\mathbf{k}_\perp|, k_\parallel) = \int U(\mathbf{k})|\mathbf{k}| \sin\Theta \, d\phi = e(|\mathbf{k}|, \Theta), \tag{6}$$

where ϕ is the longitude with respect to the x axis; then we can define [38]

$$E_V(k_\perp) = \int e(|\mathbf{k}_\perp|, k_\parallel) dk_\parallel, \tag{7}$$

$$E_V(k_\parallel) = \int e(|\mathbf{k}_\perp|, k_\parallel) dk_\perp, \tag{8}$$

$$E_V(k) = \int e(|\mathbf{k}|, \Theta)|\mathbf{k}| d\Theta. \tag{9}$$

Similar definitions hold for $h(|\mathbf{k}|, \Theta)$, the axisymmetric helicity spectrum which is based on the antisymmetric part of the velocity correlation tensor [38]. From $h(|\mathbf{k}|, \Theta)$ we then derive the definitions for $H(k)$, $H(k_\perp)$, and $H(k_\parallel)$. Similar definitions hold as well for the potential energy distribution and for the total energy distribution.

B. Numerical model

The numerical simulations are carried out using the Geophysical High-Order Suite for Turbulence (GHOST) code [39,40]. It is a pseudospectral framework available to the community and hosts a variety of partial differential equation (PDE) solvers optimized for studying turbulence in two-dimensional (2D) and three-dimensional (3D) geometries, for neutral and conducting fluids (in the magnetohydrodynamic and Hall-magnetohydrodynamic approximations), and with solid-body rotation and stratification in the Boussinesq approximation. GHOST also includes a passive scalar solver, as well as surface quasigeostrophic and shallow water solvers and several types of subgrid scale models. In the 3D case, the grid is a cubic $[0, 2\pi]^3$-periodic box, and with a second-order explicit Runge-Kutta (RK) time-stepping scheme; tests were conducted using a fourth-order explicit RK scheme that showed neither qualitative nor quantitative differences when compared with the second-order scheme at the resolutions used in this paper. Dealiasing is done by using a standard 2/3 rule. The importance of performing computations for this system in a cubic box with equal grid spacing in the horizontal and vertical directions was emphasized and demonstrated in Ref. [41]. We do not use a subgrid model and use an

explicit time-stepping method for these computations because of the necessity to resolve all spatial and time scales. For the code, a hybrid MPI-OpenMP parallelization methodology was developed [39], with tests up to 98 000 compute cores on grids of up to 6144^3 points; the code also has a third level of parallelization with the recent addition of GPU-accelerator support for the FFTs.

C. Initial conditions

A variety of runs were conducted at moderate Reynolds number in a 3D cubical domain, with isotropic discretization of $n_x = n_y = n_z = n = 256$ or $n = 512$ points. The database of the runs is presented in Table I, with parameters characterizing the initial conditions we employed. Other runs were performed that confirm the conclusions of this work but which, for the sake of brevity, are not described in detail.

Three sets of initial velocities were investigated: Taylor-Green (TG), Arnold-Beltrami-Childress (ABC), and random isotropic. The TG velocity field is given by

$$
\begin{aligned}
v_x^{\mathrm{TG}} &= v_0^{\mathrm{TG}} \sin(k_0 x) \, \cos(k_0 y) \, \cos(k_0 z), \\
v_y^{\mathrm{TG}} &= -v_0^{\mathrm{TG}} \cos(k_0 x) \, \sin(k_0 y) \, \cos(k_0 z), \\
v_z^{\mathrm{TG}} &= 0,
\end{aligned}
\tag{10}
$$

and is globally nonhelical ($\sigma_V \equiv 0$ at $t = 0$).

The ABC initial condition for the velocity is specified as

$$
\begin{aligned}
v_x^{\mathrm{ABC}} &= v_0^{\mathrm{ABC}} \left[B \cos(k_0 y) + C \sin(k_0 z) \right], \\
v_y^{\mathrm{ABC}} &= v_0^{\mathrm{ABC}} \left[C \cos(k_0 z) + A \sin(k_0 x) \right], \\
v_z^{\mathrm{ABC}} &= v_0^{\mathrm{ABC}} \left[A \cos(k_0 x) + B \sin(k_0 y) \right].
\end{aligned}
\tag{11}
$$

As a superposition of Beltrami vortices (for which $\mathbf{u} = \pm \boldsymbol{\omega}/k_0$), it is fully helical ($\sigma_V = 1$). Another approximately Beltrami initial condition was taken, namely the $\mathbf{v}^{\mathrm{ABC}}$ written above with $v_z^{\mathrm{ABC}} \equiv 0$ at $t = 0$, in order to be able to compare with the evolution of the TG flow which also has $v_z = 0$ initially. This second helical initial condition is called ABC2C (two components). The simulations were started using a superposition of these flows (TG, ABC, or ABC2C) for the wave-number interval reported in Table I.

We also examined random isotropic initial conditions (RND) [42]. The random initial velocity field is generated as follows. First, all Fourier modes with wave vector $\mathbf{k}$ such that they were in a spherical shell with $k_1 \leqslant |\mathbf{k}| \leqslant k_2$ were excited, while the rest of the modes were set equal to zero (with k_1 and k_2 being, respectively, the minimum and maximum wave numbers k_0 in Table I). In each mode in the shell, the same rms velocity was excited, but a different phase was used for each wave vector $\mathbf{k}$, obtained from a random number generator with uniform distribution. Care was taken when computing the amplitude of the x, y, and z components of the velocity for each wave number to ensure the incompressibility condition, which in Fourier space is equivalent to $\mathbf{k} \cdot \mathbf{u} = 0$. This procedure results in a random velocity field with approximately zero helicity. To control the initial value of the helicity, we used the method described in Ref. [38]. In practice, two random vector fields are created using the procedure explained above, say $\mathbf{v}_1$ and $\mathbf{v}_2$. The initial velocity field $\mathbf{u}(\mathbf{k})$ for each wave vector $\mathbf{k}$ then is obtained by correlating the velocity and the vorticity of

the two fields in the following way:

$$
\begin{aligned}
\mathbf{u}(\mathbf{k}) = v_0^{\mathrm{RND}} \{ &\cos(\alpha) \mathbf{v}_1(\mathbf{k}) + \sin(\alpha) \mathbf{v}_2(\mathbf{k}) \\
&+ \nabla \times [\sin(\alpha) \mathbf{v}_1(\mathbf{k}) + \cos(\alpha) \mathbf{v}_2(\mathbf{k})]/k \}.
\end{aligned}
\tag{12}
$$

The relative helicity of the resulting isotropic and random velocity field is then $\sin(2\alpha)$, and a random velocity field with maximal helicity (i.e., maximal velocity-vorticity correlation) is obtained therefore when $\alpha = \pi/4$.

In the expressions (10), (11), and (12), we choose $v_0^{\mathrm{TG}} = v_0^{\mathrm{ABC}} = v_0^{\mathrm{RND}} = 1$, and, for all the flows, the components of the initial velocity are multiplied by a factor f_0, such that the initial kinetic energy per unit volume is normalized to U_0^2,

$$
\frac{f_0^2}{V} \left[\int_V \left(v_x^2 + v_y^2 + v_z^2 \right) dV \right] = U_0^2.
\tag{13}
$$

Given Eq. (13) and the definition of the relative helicity, Eq. (5), the ABC flow has $\sigma_V(t = 0) = 1$, while the ABC2C flow displays $\sigma_V(t = 0) = C^2/[C^2 + (A^2 + B^2)/2]$, which, for the choice $A = 0.9$, $B = 1$, $C = 1.1$, gives $\sigma_V(t = 0) \approx 0.57$. The choice of $A \neq B \neq C$ allows for a more rapid development of the flow and for turbulence to set in by breaking more efficiently the symmetries present in the $A = B = C$ case.

The dimensionless Reynolds number Re, for the TG, ABC and random flows, are defined as

$$
\mathrm{Re}_{\mathrm{TG}} = \frac{U_0 2\pi}{k_0 \sqrt{3}\nu}, \quad \mathrm{Re}_{\mathrm{ABC,RND}} = \frac{U_0 2\pi}{k_0 \nu}.
$$

The $\sqrt{3}$ factor in the definition for the TG flow comes from the fact that the individual Fourier shells are populated in different ways, for a given k_0, for the TG vs ABC and random flows (see, e.g., Ref. [43]).

In each run the initial value of the potential temperature is $\theta(t = 0) = 0$, so buoyancy fluctuations entirely develop from the initial velocity field. Note that initial conditions need not be balanced since the time step for these runs is small enough to resolve the gravity waves that develop in each case. A reason for using balanced initial conditions is related to the fact that one may want to investigate the development of imbalanced motions to start as a result of the turbulent mixing that develops, rather than by choice of initial conditions. On the other hand, the nonlinear terms will eventually develop these unbalanced motions as nonlinear coupling takes place before and up to the peak of enstrophy.

III. RESULTS

A. The temporal decay of helicity

Here we examine the temporal behavior of the flows whose initial conditions are given in Table I. For some of the simulations, the ratio between the potential energy and the total energy at the peak of the enstrophy, the value of the relative helicity at the initial time σ_V^0, at the peak of the enstrophy, σ_V^*, and at $t = 20$, σ_V^{**}, are reported in Table II.

A hint as to the outcome one may expect from the time evolution of helicity is obtained by considering the dynamical equations. By taking the inner product of Eq. (1) with ω and volume averaging, it can be shown that the time derivative of

TABLE II. Some relevant parameters for a selected set of the runs listed in Table I. The ratio of potential to kinetic energy is given at peak of enstrophy t^*, while the relative helicity is reported at $t = 0$ (σ_V^0), at the peak of the enstrophy (σ_V^*), and at $t = 20$ (σ_V^{**}). Note the increase of relative helicity over time in all stratified cases, after an initial startup phase.

Initial v	$[E_P/E_T]^*$	σ_V^0	σ_V^*	σ_V^{**}
1. TG	0.01	0.0	0.0	0.0
6. ABCN0	0.00	0.99	0.13	0.10
7. ABC	0.15	0.99	0.22	0.76
12. RNDN0	0	1.00	0.13	0.08
13. RND	0.18	1.00	0.02	0.11
15. RND2Fr	0.18	1.00	0.04	0.13
17. RNDk2	0.17	1.00	0.11	0.70

the total helicity is

$$\frac{dH}{dt} = -2N\langle\theta\,\omega_z\rangle - 2\nu Z_H, \quad Z_H = \langle\boldsymbol{\omega}\cdot\boldsymbol{\nabla}\times\boldsymbol{\omega}\rangle, \quad (14)$$

with Z_H the helical enstrophy (sometimes called superhelicity [44]), a pseudoscalar as helicity itself. Note that, locally (as opposed to globally), helicity can be produced through alignment of vorticity and shear [45]. However, globally and for an initially helical flow, Z_H is responsible for the viscous decay of helicity. In the absence of dissipation, helicity is conserved for nonstratified flows, while the first term on the right-hand side of Eq. (14) can act as a source or a sink for stratified flows, thus breaking the conservation.

In Figs. 1(a) and 1(b) we first show the temporal evolution of the kinetic enstrophy, $Z_V(t)$, and potential enstrophy, $Z_P(t)$

(proportional to dissipation of kinetic and potential energy). All the flows have Fr ≈ 0.022, with, as initial conditions, an ABC flow, an ABC2C flow, or a TG flow. For comparison, one case with ABC initial conditions is computed with no stratification. The time in all the figures is expressed in units of the initial eddy turnover time $\tau_{\text{NL}} = 2\pi/(k_0 U_0)$. We see that the production of enstrophy, and, therefore, the transfer of energy to small scales, is *damped* substantially in the presence of stratification, both for the ABC and TG initial conditions, although its maximum is not considerably *delayed*. This is expected because the effect of waves through the buoyancy forces is to reduce the nonlinear interactions, as well as to suppress, in part, the vertical velocity component. Observe that the stratified TG flow displays a significantly stronger peak for the kinetic and potential enstrophy than the stratified ABC-like flows for which the nonlinear terms are (initially) equal to zero.

In Figs. 1(c) and 1(d) the temporal evolution of the total helicity and relative helicity for the same flows is shown. In the absence of stratification and for ABC initial conditions, helicity decays rather rapidly (exponentially after an initial nonlinear phase) and is close to zero for $t > 6$. On the contrary, the stratified ABC and ABC2C flows display slow decay of helicity, with strong oscillations at first when $v_z(t = 0) \neq 0$, linked to gravity waves. Finally, we observe that the TG flow has zero initial helicity, and none is created by stratification. It is interesting that in the stratified cases helicity decays almost linearly with time, and much more slowly than the energy, which, as will be shown later and as is often the case for turbulent flows, decays as a power law with time.

As already mentioned, in the absence of stratification the relative helicity $\sigma_V(t)$ decays rapidly, the flow becoming closer
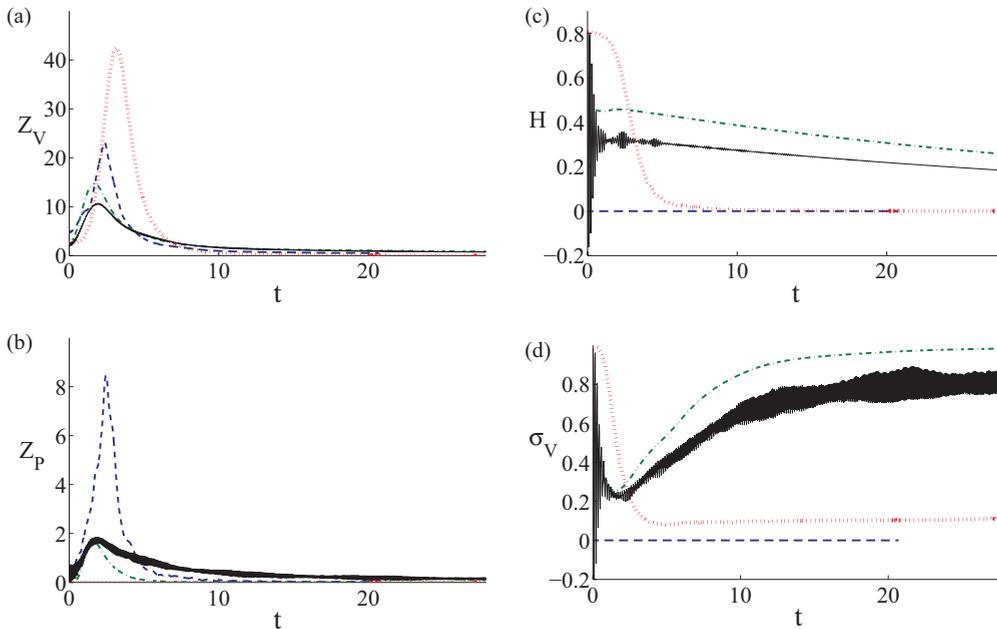

FIG. 1. (Color online) Temporal evolution of the kinetic enstrophy (a), potential enstrophy (b), total helicity (c), and relative helicity (d) for several initial conditions, namely an unstratified ABC flow (run 6, ABCN0, dotted line, red) and three flows with Fr ≈ 0.022: an ABC (run 7, solid black line), an ABC2C (run 3, dash-dotted green line), and a TG flow (run 1, dashed blue line). The helicity of the TG flow, initially zero, remains negligible (dashed blue line), whereas for the two other stratified and helical flows, the helicity decay is remarkably slow compared to the nonstratified case (dotted red line). Note the quasimaximal helical state [$\sigma_V(t) \approx 1$] reached in the ABC2C case (dash-dotted green line).
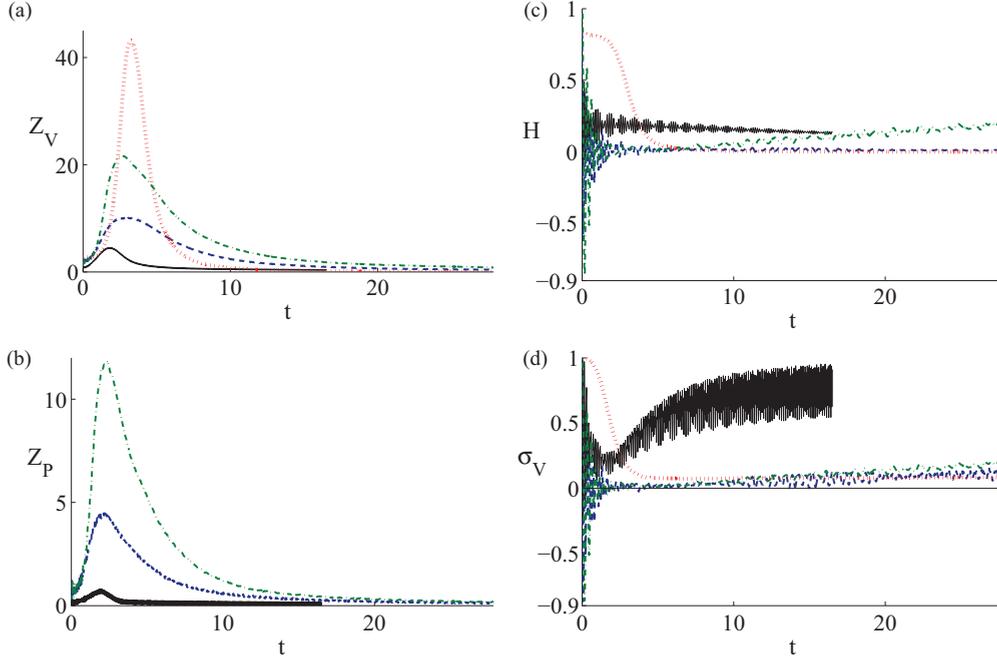
FIG. 2. (Color online) Temporal evolution of the kinetic enstrophy (a), potential enstrophy (b), total helicity (c), and relative helicity (d) for random initial conditions: an initially unstratified flow (run 12, RNDN0, dotted red line), a flow with Fr ≈ 0.022 (run 13, RND, dashed blue line), a flow with $k_0 = 2$ and Fr ≈ 0.022 (run 17, RNDk2, solid black line), and a flow with Re = 6000 and Fr ≈ 0.044 (run 15, RND2Fr, dash-dotted green line). Note that all flows are initially close to maximum helicity (see Table I).

to being mirror symmetric ($\sigma_v \approx 0$). On the other hand, when gravity is switched on and the initial helicity is nonzero, $\sigma_V(t)$ approaches its maximum possible value of unity. This may be simply due to the fact that helicity decays more slowly than energy, leading to a growth of their ratio. More precisely, it can be seen from the data shown in Fig. 1 (and later in Fig. 7) that $d_t H \ll (d_t E_V)^{1/2}(d_t Z_V)^{1/2}$, hence, in Eq. (5) the denominator increases much faster than the numerator, causing σ_V to grow.

The flows analyzed until now are well ordered, centered at large scales and with phase coherence between modes at $t = 0$. We also examined initial conditions with randomized phases, yet maintaining a high initial relative helicity (see Table II). In Figs. 2(a) and 2(b) the behavior of $Z_V(t)$ and $Z_P(t)$ for random flows with $k_0 = 3$–4 or $k_0 = 2$ is shown. It is seen that the unstratified flow displays a higher peak of the kinetic enstrophy, as noticed before, followed by the less stratified case (Fr ≈ 0.044); while, when Fr ≈ 0.022, the case with $k_0 = 2$ has a lower peak than the case with larger k_0. This is likely due to the fact that when $k_0 = 2$ the flow preserves some helicity, which inhibits the energy decay. A similar behavior is seen for the potential enstrophy: the peak is higher for the less stratified case and is lower when helicity is better preserved.

In random flows, the time evolution of the helicity and the relative helicity reveals a more complicated behavior than in ABC and TG flows. It is indeed observed that if the injection wave number is $k_0 = 2$ (as well as when $k_0 = 1$, not displayed), then, consistently with what we reported in the ABC cases, the relative helicity grows. However, as shown in Figs. 2(c) and 2(d) (see also the zoom on early-time evolution in Fig. 3), for smaller-scale initial conditions, the relative helicity decays to a value close to zero in the initial period dominated by

gravity waves. If, however, the Fr number is increased, a small growth of the relative helicity is observed also for the $k_0 = 3$–4 case. A similar run at twice the Reynolds number (using a grid with a resolution of 512^3 points) reveals no difference in the helicity behavior. The reason why random flows at $k_0 = 2$ behave similarly to ABC flows is likely due to the fact that their initial conditions resemble an ABC flow, especially with regard to the velocity distribution, with rather well-identified large-scale structures; in the case of the ABC flow, corresponding to three Beltrami waves (also called "Roberts flows"), it consists of quasiperiodic cylindrical vortices (see Ref. [46] for a visualization of the ABC flow at $t = 0$). For higher initial k_0, the randomness (and the existence of more modes that can be excited in a given Fourier shell) destroys these well-organized structures.

Different visualizations of the x and z components of the velocity, are given, respectively, in Fig. 4 and Fig. 5 for the ABC2Re and RND2Re flows (run 8 and 14, respectively, see Table I). Note that the horizontal cylindrical vortices, present in the ABC flow at $t = 0$, are being sheared and develop into a zigzag shape at the peak of dissipation, reminiscent of the zigzag instability found in laboratory experiments [47]. However, this does not appear as being as well defined in the random runs. At later times the x component of the velocity is redistributed in horizontal layers of alternating sign; this structure is much better ordered for the ABC flow but is still visible for random flows. It is clear from inspection of Fig. 5 that the vertical velocity keeps its cylindrical structuring in the ABC2Re flow, whereas it becomes more turbulent in the case of the RND2Re flow. It is also observed that, at a later stage, the ABC vertical columnar structures that survive alternate
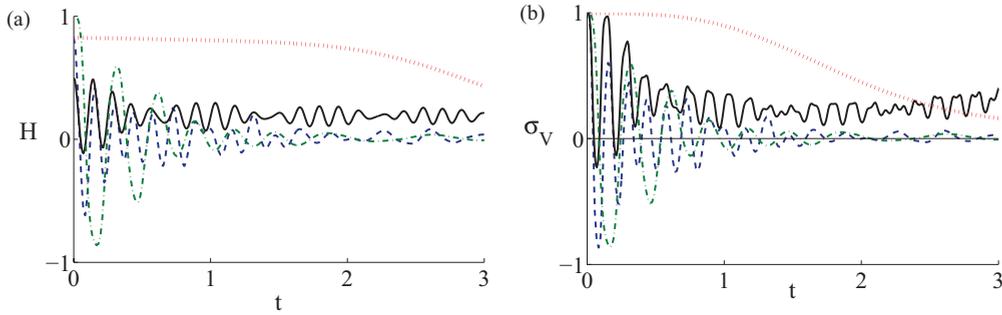
FIG. 3. (Color online) Zoom for Figs. 2(c) and 2(d) on the early-time evolution of helicity H (a) and relative helicity σ_V (b). Line labels are as described in the caption to Fig. 2.

sign in time, suggesting a coupling with internal gravity waves.

Finally, the effect of changing the Reynolds and Froude number on the time evolution of helicity for an ABC flow is shown in Fig. 6. By increasing the value of these dimensionless numbers, the total helicity increases accordingly. At fixed Froude number, the evolution appears to be slower for the higher Reynolds number, whereas at fixed Reynolds number, the decay of helicity appears to be independent of Froude number. This would indicate that helicity dynamics is not governed solely by stratification but rather more strongly by dissipation (see also the discussion in the next subsection). The same phenomenon is observed, even if in smaller proportion, in the case of random flows.
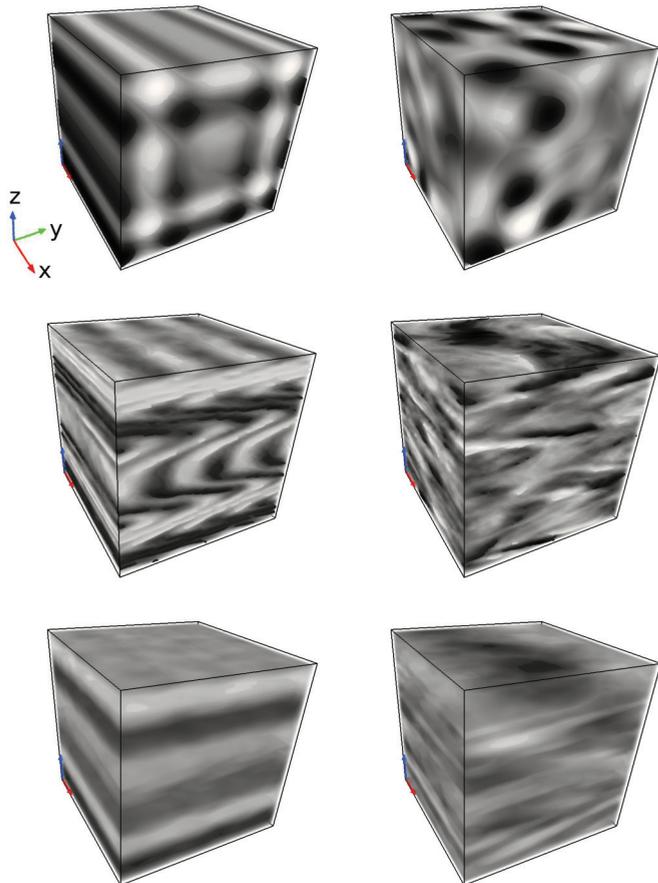
FIG. 4. (Color online) Distribution of the x (horizontal) velocity v_x for the ABC2Re flow (run 8, left) and the RND2Re flow (run 14, right) at times (from top to bottom) $t = 0$, $t = t^*$ (i.e., at the peak of dissipation), and $t = 20$. Light corresponds to low negative values, dark to high positive values. The vertical direction is indicated by the upward (blue) arrow. The three axes are shown separately. Observe the strong shear layers that have developed by the peak in dissipation and which later on begin to smooth out.
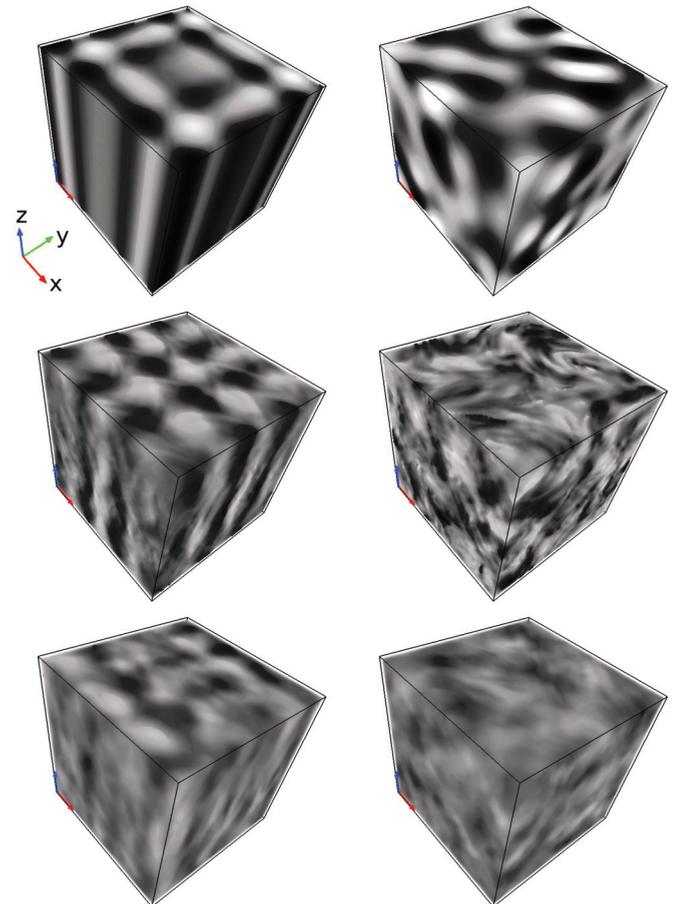

FIG. 5. (Color online) Distribution of the vertical velocity v_z for the ABC2Re flow (run 8, left) and the RND2Re flow (run 14, right) at times (from top to bottom) $t = 0$, $t = t^*$, and $t = 20$. Light corresponds to low negative values, dark to high positive values. Observe the more turbulent flow in the random case at t^*.
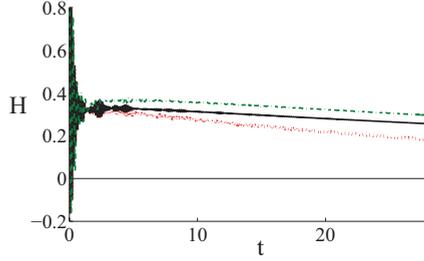
FIG. 6. (Color online) Temporal evolution of the total helicity for ABC flows with Re = 6000 and Fr = 0.022 (run 8, ABC2Re, solid black line), Re = 6000 and Fr = 0.044 (run 9, ABC2Fr, dashed-dotted green line), and Re = 3000 and Fr = 0.022 for reference (run 7, ABC, dotted red line). The decay of helicity is slower at higher Reynolds number for the same Froude number, whereas it is comparable for both Froude numbers for the same Reynolds number.

B. Cyclostrophic balance

By measuring separately the first and second terms on the right-hand side of the dH/dt expression given in Eq. (14), we find that, at early times, characterized by high-amplitude gravity waves, the first term dominates. After the peak of enstrophy, the two terms are small and balanced and cause $dH/dt \approx 0$. For the ABC2C flow with $v_z(t = 0) = 0$, there is no need for radiation of gravity waves to adjust to large-scale balance and the two terms are small and comparable at all times. This may explain the large values of residual helicity at late stages.

We observe that both the ABC and the random $k_0 = 2$ flows initially excite smaller amplitude oscillations of the first term of Eq. (14) than do the $k_0 = 3$–4 random flows. These oscillations cease roughly at the peak of the enstrophy, when nonlinear coupling of waves takes over the linear phase. If the oscillation amplitude is large, $H(t)$ goes to zero even before the peak of enstrophy (this is observed for the $k_0 = 3$–4 random flows), an irremediable situation in the case of decaying flows, while, if the oscillation amplitude is small, $H(t)$ will have a nonzero residual value at the peak of enstrophy, and from there on it will decay very slowly (ABC and $k_0 = 2$ random cases).

Increasing the Reynolds number does not seem to modify the behavior of $H(t)$ before the peak of the enstrophy, because the dynamical evolution in this first stage is plausibly wave dominated. If the Froude number is varied instead, from Fr = 0.022 to Fr = 0.044, the initial oscillations are reduced and now the random case with $k_0 = 3$–4 also sees a growth of the relative helicity (see Fig. 2). We have to conclude that the growth of relative helicity, or, similarly, the slow decay of helicity, is nonmonotonic with Froude number since in the case $N = 0$, a decay of $\sigma_V(t)$ is observed. Another distinction which may help interpreting the different behavior of helicity in the ABC flow and the random flow, is that while in ABC flows helicity is organized in large-scale coherent structures, in the structureless random flow it is not (except for $k_0 = 2$).

We are thus led to conjecture that, similarly to the geostrophic balance in rotating stratified turbulence, another large-scale balance, linked to dissipation, can take place in helical flows in the presence of stratification alone. Such *viscous cyclostrophic balance* would be consistent with $dH/dt \approx 0$, as observed for the Froude numbers considered. By neglecting

the time derivative and the nonlinear term in Eq. (1), taking the curl of the reduced equation and dotting it with velocity, we arrive at the following balance equation:

$$N\mathbf{u} \cdot \mathbf{\nabla} \times (\theta \, e_z) = -\nu\mathbf{u} \cdot \nabla^2\boldsymbol{\omega} = \nu\mathbf{u} \cdot \mathbf{\nabla} \times \mathbf{\nabla} \times \boldsymbol{\omega}. \quad (15)$$

Note that at this stage, there is no space average being computed; however, upon space integration, this gives the relationship between the product of temperature and vertical vorticity and the super helicity, as derived before, a balance that may hold at large scales where the waves dominate the dynamics. This balance cancels the two terms on the right-hand side of Eq. (14), thus explaining the slow decay of helicity when it is initially at large scales. What happens with this balance when the buoyancy Reynolds number is increased will require runs at higher resolution (or lower stratification) than what is considered in the present paper and will be the topic of a subsequent study (see Ref. [25] for a large run where the Ozmidov scale is clearly resolved). However, it is interesting to note that viscous forces are known to play other important roles in stratified turbulence, such as when gravity waves break and alter the conservation of total energy and of potential vorticity, leading to the creation of dipones in V_{pot} (see Ref. [48]).

C. Energy decay

We now turn our attention to the temporal evolution of energy. We display in Figs. 7 and 8 the decay of the total energy for a variety of initial conditions and Froude numbers (see captions for details). Computations are performed for roughly 30 turnover times (and, thus, for 3000 Brunt-Väisällä periods, for Fr = 0.01); some power laws are added to guide the eye. When examining separately the temporal decay of the potential and kinetic energy, they evolve in similar ways but with strong oscillatory energy exchanges, while the oscillations due to gravity waves disappear when considering the total energy.

In Fig. 7 it is striking to notice that the decay of energy can be very different for different flows with the same external parameters (i.e., Reynolds and Froude numbers). If t^* is the time at which dissipation sets in, that is, the maximum of enstrophy, the decay in the absence of stratification would
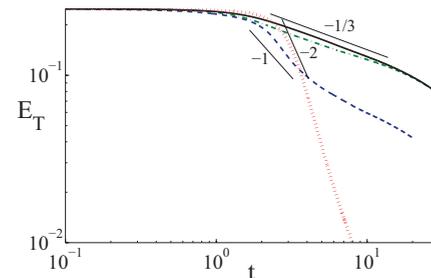

FIG. 7. (Color online) Temporal evolution of the total energy, with different scaling laws given as indications. ABC flow (run 7, solid black line), ABC2C flow (run 3, dash-dotted green line), and TG flow (run 1, dashed blue line), the latter two having initially $v_z = 0$. All runs have Re ≈ 3000 and Fr ≈ 0.02 except for the ABC flow with $N = 0$ which is shown for comparison with a dotted (red) line (run 6, ABCN0). Note the particularly slow decay for ABC runs 3 and 7.
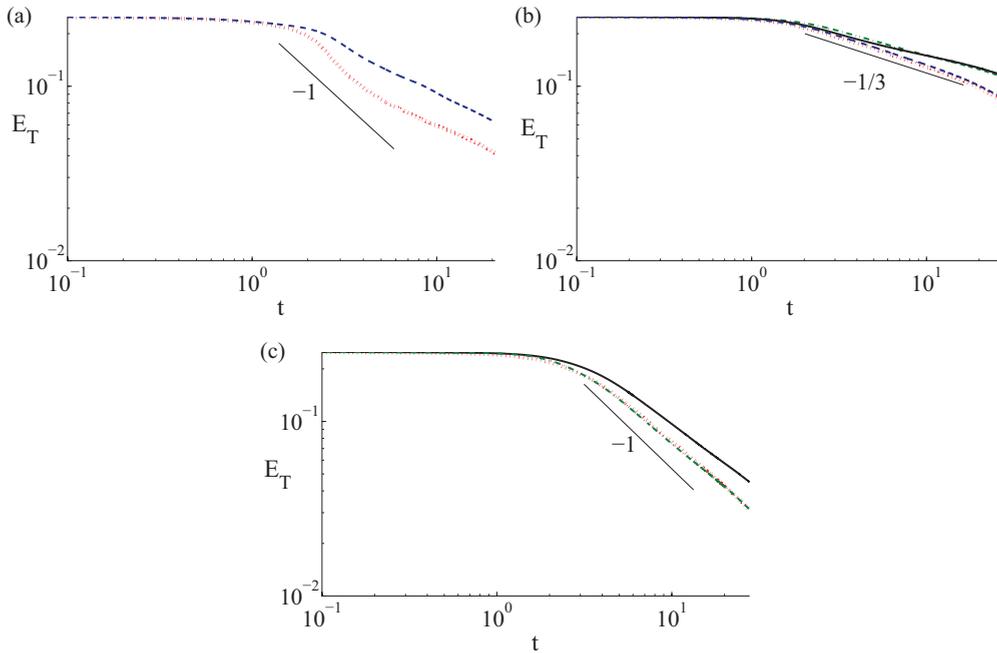
FIG. 8. (Color online) Temporal evolution of the total energy $E_T(t)$, with different scaling laws given as indications for (a) TG flows at different Froude numbers, Fr ≈ 0.011 (run 2, dashed blue line) and Fr ≈ 0.022 (run 1, dotted red line); (b) ABC flows with Re = 6000 and Fr = 0.022 (run 8, dash-dotted green line), Re = 6000 and Fr = 0.044 (run 9, solid black line), Re = 3000 and Fr = 0.011 (run 11, dashed blue line), and Re = 3000 and Fr = 0.022 (run 7, dotted red line); (c) random flows with Re = 6000 and Fr = 0.022 (run 14, solid black line), Re = 6000 and Fr = 0.044 (run 15, dash-dotted green line), and Re = 3000 and Fr = 0.022 for reference (run 13, dotted red line). Note the significantly slower decay in (b) for the case of the ABC flows.

follow a $\sim (t^* - t)^{-2}$ law (dotted line) given that the growth of the integral scale is prevented by being in a "box-limited" case, that is, $k_0 \approx k_{\min} = 1$. Considering the nonhelical TG flow, the decay seems to follow a power law $\sim(t^* - t)^{-1}$, after an initial ideal (inviscid) phase. This result is expected on the basis of the slow-down of nonlinear interactions (leading to energy transfer and its decay) because of waves, and a similar power-law decay has already been observed for stratified flows [24], for rotating flows [49], as well as for flows in the presence of a magnetic field [50]. For the ABC stratified flow, the decay of energy is substantially slower, with a power law of $-1/3$ as opposed to -1. On the other hand, we recall that helicity decays linearly and at a very slow rate, as shown in the preceding section (see Fig. 1 and Fig. 2).

The slow decay of energy has been observed previously for rotating turbulence in the presence of helicity and the different power laws one may expect have been reviewed for a variety of cases taking into account the invariance of both energy and helicity [51]. A $(t^* - t)^{-1/3}$ law is found on phenomenological grounds for helical rotating flows based on the fact that helicity plays a role in the dynamics: It dominates the energy transfer to small scales and alters the spatial scaling laws for the energy spectra and for higher-order structure functions as well [52,53] (see also Ref. [54] for a review). The similar decay law found in this paper for ABC-like stratified flows may be due to the fact that, as shown here, the helicity is quasiconserved by the dynamics, due to a cyclostrophic balance, and, thus, leads to the same slow decay. We thus conclude that, for flows with either rotation or stratification, the presence of helicity considerably slows down the energy decay, and measurably

so, leading to persistent structures, whereas for the unstratified nonrotating case, helicity delays the onset of the decay but does not alter its rate of decay [51].

In Fig. 8 we examine the possible variation of the decay rate of energy with several factors: Froude and Reynolds numbers, as well as TG, ABC, and random initial conditions. We observe that, for the TG flow, the decay is first faster ($\sim t^{-1}$) and then slows down; this could be due to the fact that, as time evolves and energy decays, the Froude number of a given flow becomes substantially smaller; note that the later decay in Fig. 8(a) corresponds to an exponential regime, as can be easily verified, displaying the data in lin-log coordinates (not shown). If the Froude number is decreased the decay is delayed (dashed-line), while still following the same power law. A similar effect is observed for ABC flows in Fig. 8(b) where results for two different Reynolds numbers are reported: the higher the Reynolds number, the shallower the energy decay.

For the random cases [Fig. 8(c)], when $k_0 = 3$–4, helicity has become negligible by the peak of the enstrophy, as previously observed, and the decay follows an approximate t^{-1} law. When $k_0 = 2$ there are too few modes to excite in building a random initial condition, and at early times the randomness of such flows is rather weak, with well-ordered columns in the initial conditions, reminiscent of the ABC flow itself (see, e.g., Fig. 4). Helicity then does not go to zero, and the decay follows, as in the ABC case, a $-1/3$ power law (this case is not shown).

In general terms, it seems reasonable to conclude that, for stratified flows, if helicity vanishes by the time of occurrence of the peak of the enstrophy, the decay will follow a -1 power

law, while if the initial helicity value is high and it survives up until the maximum of dissipation, the decay will follow a $-1/3$ power law.

D. Energy and helicity spectra

The effect of strong and large-scale helicity on the temporal decay rate of the total energy is, thus, striking. We now address the related question of the possible role of helicity on energy distribution among Fourier modes. In the anisotropic case, the analysis becomes quite arduous since one has to consider the Fourier decomposition along perpendicular and parallel directions (referring to the imposed stratification in the vertical), and the spectra of kinetic and potential energy and of helicity. Note that other decompositions of the data have been advocated in the literature (see Refs. [14,55] and Ref. [4] for a recent exposition); indeed, because of incompressibility, two scalar functions suffice to define the kinetic energy spectra and a commonly used decomposition is that in toroidal and poloidal modes.

In Fig. 9 we show the isotropic (k), parallel ($k_\parallel$), and perpendicular ($k_\perp$) total energy spectra, E_T, together with the parallel and perpendicular potential energy spectra, E_P, for four ABC flows with different Froude and Reynolds numbers (see caption). The spectra are plotted at the peak of enstrophy t_* and are averaged over ≈ 0.3–0.4 eddy turnover times after t_*. As general remarks, we note that the energy is rather strongly peaked at k_0, and we observe that, at high wave numbers, the spectra are more developed when the Froude number is higher, since nonlinear interactions are comparatively more efficient. The survival of the initially excited large scales is expected, since both wave interactions and helicity can inhibit the energy transfer to smaller scales. This fact may explain the rather shallow spectrum at intermediate wave numbers, followed by the very steep spectrum at high wave numbers, observed in Figs. 9(a) and 9(b). In the isotropic energy spectrum [Fig. 9(a)], the transition between the rather flat behavior and the steep high-wave-number scaling law is marked by a "knee" around $k \approx 30$, which is possibly coincident with the buoyancy wave number k_b: $k_b \approx 25$ for Fr $= 0.022$ and $k_b \approx 13$ for Fr $= 0.044$. The same sharp break is observed in the total and potential parallel energy spectra; it seems entirely attributable to the behavior of the flow with respect to variations in the vertical direction, a fact that strengthens its identification with k_b.

The perpendicular spectra consistently behave with a k^{-3} power law, as found in several numerical studies for this parameter regime [2,56].

Flat spectra have already been documented in the literature for stratified turbulence and various interpretations have been provided. A flat energy spectrum has been derived in Ref. [24] on the basis of a superposition of independent horizontal layers, each with a Gaussian profile, as a model of the vertically sheared horizontal layers associated with the zigzag instability [47] (as well as with geostrophic balance when one takes rotation into account). Indeed, the thickness of these layers is thought to be the buoyancy scale, as advocated in [47] using a scaling argument that states that the Froude number based on a vertical length scale has to be of order unity. This has already been studied in a series of direct numerical simulations (see,
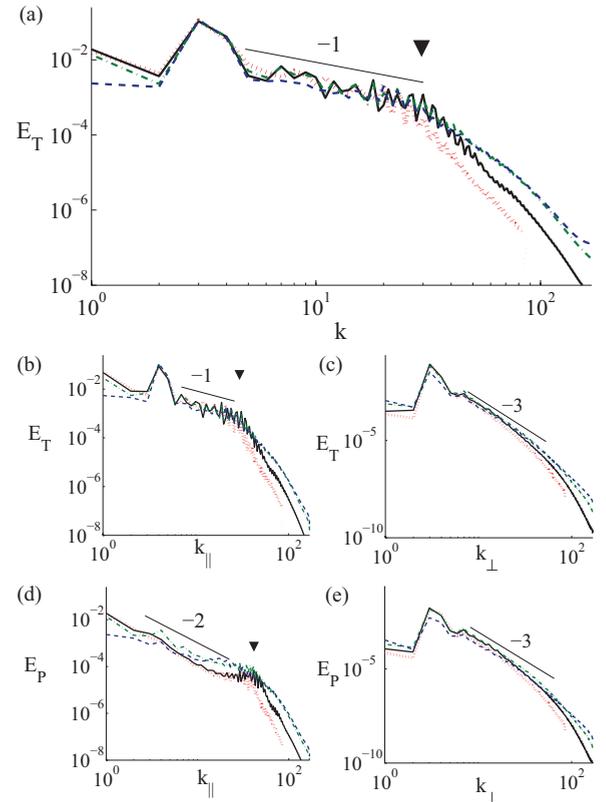

FIG. 9. (Color online) Isotropic (a), parallel (b), and perpendicular (c) total energy spectra and parallel (d) and perpendicular (e) potential energy spectra for ABC flows with Re $= 6000$ and Fr $= 0.022$ (run 8, solid black line), Re $= 6000$, and Fr $= 0.044$ (run 9, dash-dotted green line), Re $= 6000$ and Fr $= 0.088$ (run 10, dashed blue line), and Re $= 3000$ and Fr $= 0.022$ (run 7, dotted red line). Slopes are indicated as a reference. In this and subsequent figures, a black arrow indicates a sharp break (or knee) in the spectra. Note that the rather flat spectrum in the total energy stems from vertical variations [(b) and (d)], whereas the perpendicular spectra [(c) and (e)] are close to a $k_\parallel^{-3}$ scaling for all values of parameters.

e.g., Refs. [16,41] for more details). Here we hypothesize that flat spectra may be related to the presence of high helicity values as we discuss below commenting on Fig. 10.

The knee we have identified in the evolution of energy spectra (indicated by a black arrow in the figures) as a function of $k_\parallel$ is also not a new feature of stratified turbulence. It has been attributed to a change of regime for the total energy (or its horizontal component) at high resolution (specifically with the dissipation wave number sufficiently resolved) at the buoyancy scale [57]. On the other hand, in Ref. [56], both the wave mode (corresponding to the vertical velocity) and the vortex mode (corresponding to the horizontal velocity) display a sharp break in terms of $k_\parallel$ for highly stratified flows, identified as the buoyancy scale. Our data lead us to argue (see below) that another, rather independent, phenomenon may be happening as well, namely the role played by the helicity distribution among modes.

The isotropic, parallel, and perpendicular helicity spectra are shown in Fig. 10 for the same ABC flows (note that the absolute value of helicity is displayed). Similarly to the total
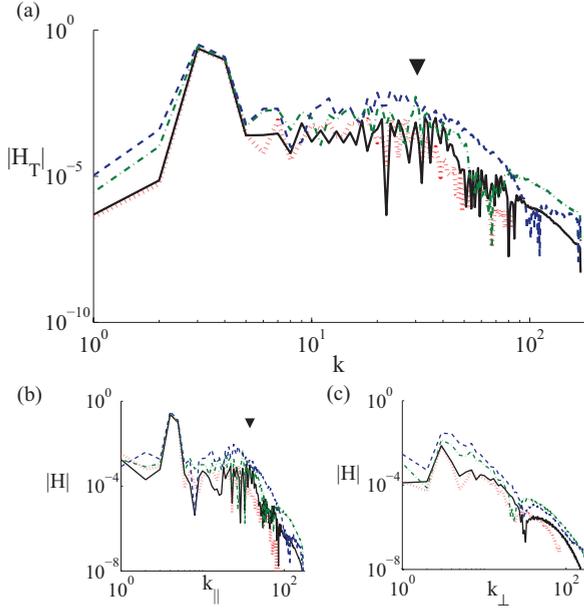
FIG. 10. (Color online) Isotropic (a), parallel (b), and perpendicular (c) helicity spectra for the same flows as in Fig. 9: run 8 (solid black line), run 9 (dash-dotted green line), run 10 (dashed blue line), and run 7 (dotted red line). Note the flat spectra at large scales, stemming again from vertical variations. Such flat spectra have been observed in the nocturnal planetary boundary layer [35]. The arrows highlight a sharp break in the spectra discussed in the text.

and parallel isotropic energy spectra are the following points: (i) the spectrum is flat at large scale and (ii) a knee is present for the total and parallel helicity. In addition we also observe a secondary change in the spectra at a smaller scale which seems to coincide with a change of sign of helicity. Since, according to the Schwartz inequality we have $H(k) \leqslant kE_V(k)$, and since helicity is large for these flows, it is reasonable to think that the behavior of the energy spectra in these runs is influenced by the behavior of helicity.

As the temporal data indicates that the ABC flow behaves differently from random flows, we now examine the spectral behavior for the random case. In Fig. 11 the energy spectra for random flows centered initially on wave number $k_0 = 3,4$ are presented. We recall that at the peak of enstrophy, the residual helicity is close to zero for these runs. In these cases, there is no clear signature of an abrupt slope change for the energy. The higher the Re and Fr numbers, the shallower the spectra at small scales. The peak at k_0 is also noticeably reduced with respect to the ABC cases, indicating more efficient energy transfer from the energy-containing scales.

Finally, in Fig. 12, the helicity spectra for the random cases initially centered at $k_0 = 3$ and 4 are shown. The value of helicity is much smaller than for the ABC runs, as noted in Table II: The residual relative helicity σ_V at the peak of enstrophy is close to 2%, whereas for the ABC runs it is close to 20%. At the end of the runs, these values are, respectively, $\approx 11\%$ and $\approx 80\%$, i.e., almost as strong as it can be in the latter case. A slope change (sharp break) is still identifiable at a wave number again comparable to the buoyancy wave number k_b, in particular in the parallel spectra, but the helicity is now too weak to significantly influence the behavior of
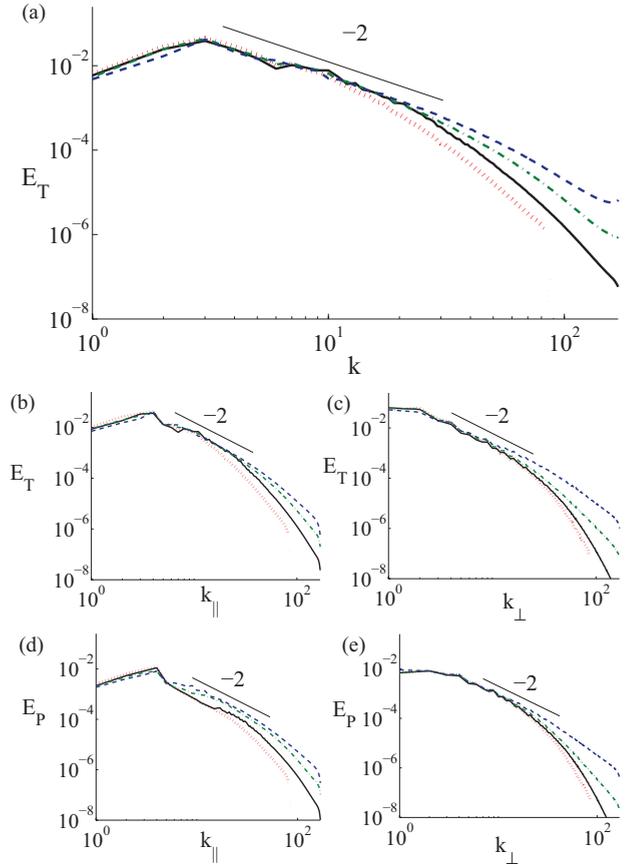

FIG. 11. (Color online) Isotropic (a), parallel (b), and perpendicular (c) total energy spectra, and parallel (d) and perpendicular (e) potential energy spectra for random flows with Re = 6000 and Fr = 0.022 (run 14, solid black line), Re = 6000 and Fr = 0.044 (run 15, dash-dotted green line), Re = 6000 and Fr = 0.088 (run 16, dashed blue line), and Re = 3000 and Fr = 0.022 (run 13, dotted red line). Slopes are indicated as a reference. No knee (sharp break in the slope) in the spectra is discernible, contrary to ABC flows.

the energy spectrum. Note also that at scales larger than the buoyancy scale (but smaller than the initial condition scale), the helicity spectrum is again flat, likely due to the layered structure in the vertical, whereas the perpendicular spectrum is steep. Only for Run 16 with the highest Froude number is there a noticeable departure from a flat spectral law. This remark can be used in interpreting the recent data on helicity spectra in the atmosphere. Indeed, we note that, at night when the planetary boundary layer is more stable, flat spectra for the helicity have been clearly identified as well [35].

To conclude, it seems likely, for helical flows here represented by ABC initial conditions, that it is the helicity which is responsible for the change of slope in the energy spectrum close to the buoyancy scale. Assuming that the Schwarz inequality is fulfilled, a flat helicity spectrum leads to $E_V(k) \sim k^{-1}$, compatible with what we observe for the energy in the ABC case. A similar result obtains for the random initial condition centered on $k_0 = 2$. This point will need further studies at high resolution so different energy and helicity balance can take place in flows with sufficient scale separation.
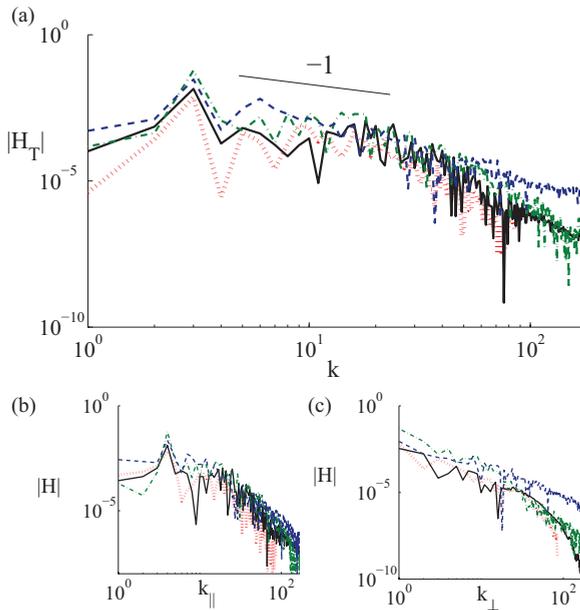
FIG. 12. (Color online) Isotropic (a), parallel (b), and perpendicular (c) helicity spectra for the same random flows as in Fig. 11: run 14 (solid black line), run 15 (dash-dotted green line), run 16 (dashed blue line), and run 13 (dotted red line).

IV. CONCLUSION

We have performed numerical simulations of strongly stratified turbulence (see Table I for parameters) imposing both helical and nonhelical initial conditions and we have shown that when helicity is preserved at large scales it produces measurable effects. This is observable in both the energy decay, which is found to be substantially slower in the helical case, and in the energy spectra, which, for helical flows, display a flat distribution with a sharp break in spectral slope in the vicinity of the buoyancy scale L_b. Beyond L_b, the spectra are significantly steeper. These knees are clearly identified in the parallel spectra and seem to be close to the buoyancy scale, in agreement with the interpretation of L_b as the scale at which Fr ≈ 1.

Thus, for helical stratified turbulence, the energy decay is slowed down by the presence of helicity in a way reminiscent to that observed in the rotating case. However, it should be noted that helicity is an ideal invariant of rotating flows,

whereas it is not *a priori* conserved for ideal stratified flows. While in the former case the slow-down in the decay is associated with a direct cascade of the helicity, in the latter case a very slow (linear in time) decay of helicity (resulting in a quasiconservation) can be attributed to a cyclostrophic balance where dissipation and gravity equilibrate at large scales once the nonlinear terms start transferring energy to small scales after an initial wave-dominated regime. These results are obtained in cases where the evolution of large scales is somewhat inhibited, because the initial scale of the flow is comparable to the overall size of the computational box, the so-called box-limited conditions in which the growth of the integral scale is blocked.

Moreover, in highly turbulent flows such as those found in geophysics and astrophysics, the eddy turnover time becomes shorter than τ_W at smaller scales, for a sufficiently large Reynolds number. In that case, isotropic turbulence may recover, beyond the so-called Ozmidov scale $L_{oz} \sim [\epsilon/N^3]^{1/2}$. Assuming further that this scale is larger than the dissipation scale $\ell_{diss} \sim [\epsilon/\nu^3]^{1/4}$ leads to the condition that the buoyancy Reynolds number $\mathcal{R} = \mathrm{Re}\mathrm{Fr}^2$ be larger than unity. It was found recently that power laws of the energy spectra scale with $\mathcal{R}$, as opposed to the Froude number itself [58]. The condition $\mathcal{R} \gg 1$ is easily fulfilled in geophysical flows but difficult to realize in numerical simulations, where the highest to-date resolution (and, thus, scale separation) is found in Ref. [25], realized on a grid of $4096^2 \times 2048$ points; similarly, laboratory experiments function at moderate $\mathcal{R}$ [59]. Further studies of that regime are necessary but will require substantial numerical resources.

[1] J. J. Riley and M.-P. Lelong, Annu. Rev. Fluid Mech. **32**, 613 (2000).

[2] C. Staquet and J. Sommeria, Annu. Rev. Fluid Mech. **34**, 559 (2002).

[3] L. Liechtenstein, F. S. Godeferd, and C. Cambon, J. Turbulence **6**, N24 (2005).

[4] P. Sagaut and C. Cambon, *Homogeneous Turbulence Dynamics* (Cambridge University Press, Cambridge, UK, 2008).

[5] W. Peltier and C. Caulfield, Annu. Rev. Fluid Mech. **35**, 135 (2003).

[6] G. Ivey, K. Winters, and J. Koseff, Annu. Rev. Fluid Mech. **40**, 169 (2008).

[7] P. Embid and A. Majda, Geophys. Astrophys. Fluid Dyn. **87**, 1 (1998).

[8] K. Julien, E. Knobloch, R. Milliff, and J. Werne, J. Fluid Mech. **555**, 233 (2006).

[9] A. J. Majda, M. Mohammadian, and Y. Xing, GAFD **102**, 543 (2008).

[10] R. Klein, Annu. Rev. Fluid Mech. **42**, 249 (2010).

[11] I. Grooms, K. Julien, J. B. Weiss, and E. Knobloch, Phys. Rev. Lett. **104**, 224501 (2010).

[12] B. A. Wingate, P. Embid, M. Holmes-Cerfon, and M. A. Taylor, J. Fluid Mech. **676**, 546 (2011).

[13] K. Julien, A. M. Rubio, I. Grooms, and E. Knobloch, Geophys. Astrophys. Fl. Dyn. **106**, 392 (2012).

[14] F. Godeferd and C. Cambon, Phys. Fluids **6**, 2084 (1994).

[15] C. Staquet and F. Godeferd, J. Fluid Mech. **360**, 295 (1998).

[16] F. Godeferd and C. Staquet, J. Fluid Mech. **486**, 115 (2003).

[17] S. Nazarenko, *Wave Turbulence*, Vol. 825 (Springer-Verlag, Berlin, 2011).

[18] A. Newell and B. Rumpf, Annu. Rev. Fluid Mech. **59**, 59 (2011).

[19] P. Caillol and V. Zeitlin, Dyn. Atm. Ocean **32**, 81 (2000).

[20] F. Bretherton, J. Fluid Mech. **20**, 457 (1964).

[21] C. McComas and F. Bretherton, J. Geophys. Res. **82**, 1397 (1977).

[22] A. Majda and E. Tabak, Physica D **96**, 515 (1996).

[23] M. Molemaker, J. McWilliams, and X. Capet, J. Fluid Mech. **654**, 35 (2010).

[24] Y. Kimura and J. Herring, J. Fluid Mech. **328**, 253 (1996).

[25] S. Almalkie and S. M. de Bruyn Kops, J. Turb. **13**, N29 (2012).

[26] C. Wunsch and R. Ferrari, Annu. Rev. Fluid Mech. **36**, 281 (2004).

[27] P. MacCready and W. R. Geyer, Ann. Rev. Marine Sci. **2**, 35 (2010).

[28] A. Brandenburg and K. Subramanian, Phys. Rep. **417**, 1 (2005).

[29] F. Godeferd and L. Lollini, J. Fluid Mech. **393**, 257 (1999).

[30] E. Rassmussen and D. Blanchard, Weather Forecast **13**, 1148 (1998).

[31] G. Levina and M. Montgomery, Dokl. Earth Sci. **434**, 1285 (2010).

[32] P. M. Markowski, J. M. Straka, E. N. Rasmussen, and D. O. Blanchard, Mont. Weath. Rev. **126**, 2959 (1998).

[33] Y. Xu and R. Wu, Adv. Atm. Phys. **20**, 940 (2003).

[34] W. P. Winn, S. J. Hunyady, and G. D. Aulich, J. Geophys. Res. **104**, 22067 (1999).

[35] B. Koprov, V. Koprov, V. Ponomarev, and O. Chkhetiani, Dokl. Phys. **50**, 419 (2005).

[36] R. Marino, P. Mininni, D. Rosenberg, and A. Pouquet, Phys. Rev. E **87**, 033016 (2013).

[37] H. Moffatt and A. Tsinober, Annu. Rev. Fluid Mech. **24**, 281 (1992).

[38] P. D. Mininni, D. Rosenberg, and A. Pouquet, J. Fluid Mech. **699**, 263 (2012).

[39] P. D. Mininni, D. Rosenberg, R. Reddy, and A. Pouquet, Parallel Comput. **37**, 316 (2011).

[40] D. O. Gómez, P. D. Mininni, and P. Dmitruk, Phys. Scr., T **116**, 123 (2005).

[41] M. Waite and P. Bartello, J. Fluid Mech. **517**, 281 (2004).

[42] A. Pouquet and G. S. Patterson, J. Fluid Mech. **85**, 305 (1978).

[43] A. Sen, P. D. Mininni, D. Rosenberg, and A. Pouquet, Phys. Rev. E **86**, 036319 (2012).

[44] R. Hide, Q. J. Roy. Met. Soc. **128**, 1759 (2002).

[45] W. H. Matthaeus, A. Pouquet, P. D. Mininni, P. Dmitruk, and B. Breech, Phys. Rev. Lett. **100**, 085003 (2008).

[46] T. Dombre, U. Frisch, J. M. Greene, M. Hénon, A. Mehr, and A. M. Soward, J. Fluid Mech. **167**, 353 (1986).

[47] P. Billant and J.-M. Chomaz, Phys. Fluids **13**, 1645 (2001).

[48] P. Haynes and M. McIntyre, J. Atmosph. Sci. **42**, 2021 (1990).

[49] T. Teitelbaum and P. D. Mininni, Phys. Rev. Lett. **103**, 014501 (2009).

[50] S. Galtier, H. Politano, and A. Pouquet, Phys. Rev. Lett. **79**, 2807 (1997).

[51] T. Teitelbaum and P. D. Mininni, Phys. Fluids **23**, 065105 (2011).

[52] P. Mininni and A. Pouquet, Phys. Fluids **22**, 035105 (2010).

[53] P. Mininni and A. Pouquet, Phys. Fluids **22**, 035106 (2010).

[54] A. Pouquet and P. Mininni, Philos. Trans. R. Soc. **368**, 1635 (2010).

[55] P. Bartello, J. Atmos. Sci. **52**, 4410 (1995).

[56] Y. Kimura and J. R. Herring, J. Fluid Mech. **698**, 19 (2012).

[57] M. L. Waite, Phys. Fluids **23**, 066602 (2011).

[58] P. Bartello and S. Tobias [J. Fluid Mech. (to be published)].

[59] M. L. Waite, *Modeling Atmospheric and Oceanic Flows: Insights from Laboratory Experiments and Numerical Simulations* edited by T. von Larcher and P. Williams (American Geophysical Union, Washington, DC (in press)).